NEOPLASIA
www.neoplasia.com

Volume 11 Number 3 March 2009 pp. 247–259 247

Noninvasive Multimodality Imaging of the Tumor Microenvironment: Registered Dynamic Magnetic Resonance Imaging and Positron Emission Tomography Studies of a Preclinical Tumor Model of Tumor Hypoxia[1,2]

HyungJoon Cho*, Ellen Ackerstaff*, Sean Carlin*, Mihaela E. Lupu*, Ya Wang*, Asif Rizwan*, Joseph O'Donoghue*, C. Clifton Ling*, John L. Humm*, Pat B. Zanzonico* and Jason A. Koutcher*,†,‡

*Departments of Medical Physics, †Radiology and ‡Medicine, Memorial Sloan-Kettering Cancer Center, New York, NY 10065, USA

Abstract

In vivo knowledge of the spatial distribution of viable, necrotic, and hypoxic areas can provide prognostic information about the risk of developing metastases and regional radiation sensitivity and may be used potentially for localized dose escalation in radiation treatment. In this study, multimodality *in vivo* magnetic resonance imaging (MRI) and positron emission tomography (PET) imaging using stereotactic fiduciary markers in the Dunning R3327-AT prostate tumor were performed, focusing on the relationship between dynamic contrast-enhanced (DCE) MRI using Magnevist (Gd-DTPA) and dynamic ^{18}F-fluoromisonidazole (^{18}F-Fmiso) PET. The noninvasive measurements were verified using tumor tissue sections stained for hematoxylin/eosin and pimonidazole. To further validate the relationship between ^{18}F-Fmiso and pimonidazole uptake, ^{18}F digital autoradiography was performed on a selected tumor and compared with the corresponding pimonidazole-stained slices. The comparison of Akep values (kep = rate constant of movement of Gd-DTPA between the interstitial space and plasma and A = amplitude in the two-compartment model (Hoffmann U, Brix G, Knopp MV, Hess T and Lorenz WJ (1995). *Magn Reson Med* **33**, 506–514) derived from DCE-MRI studies and from early ^{18}F-Fmiso uptake PET studies showed that tumor vasculature is a major determinant of early ^{18}F-Fmiso uptake. A negative correlation between the spatial map of Akep and the slope map of late (last 1 hour of the dynamic PET scan) ^{18}F-Fmiso uptake was observed. The relationships between DCE-MRI and hematoxylin/eosin slices and between ^{18}F-Fmiso PET and pimonidazole slices confirm the validity of MRI/PET measurements to image the tumor microenvironment and to identify regions of tumor necrosis, hypoxia, and well-perfused tissue.

Neoplasia (2009) 11, 247–259

Abbreviations: DAR, digital autoradiography; DCE-MRI, dynamic contrast-enhanced magnetic resonance imaging; Fmiso, fluoromisonidazole; FOV, field of view; FWHM, full-width half-maximum; H&E, hematoxylin/eosin; MRI, magnetic resonance imaging; NA, number of averages; NR, number of repetitions; PET, positron emission tomography; ST, slice thickness; TE, echo time; TR, repetition time

Address all correspondence to: Ellen Ackerstaff, Memorial Sloan-Kettering Cancer Center, 1275 York Avenue, New York, NY 10065. E-mail: ackerste@mskcc.org

[1]This research was supported by National Institutes of Health (NIH) grant no's. PO1 CA115675 and P50 CA86438. This publication acknowledges National Cancer Institute grant number P30 CA08748, which provides partial support for the Research Animal Resource Center, the Radiochemistry Core, and the Small-Animal Imaging Core at Memorial Sloan-Kettering Cancer Center (MSKCC), and the NIH Small-Animal Imaging Research Program (SAIRP) grant no. R24 CA83084, which provides partial support for the Small-Animal Imaging Core at MKSCC.

[2]This article refers to supplementary materials, which are designated by Figures W1 and W2 and are available online at www.neoplasia.com.

Received 24 October 2008; Revised 20 December 2008; Accepted 22 December 2008

DOI 10.1593/neo.81360

Introduction

It is anticipated that the ability to image the tumor microenvironment *in vivo* will provide useful prognostic information including an assessment of factors that influence response to treatment. For example, hypoxia, typically distributed heterogeneously in locally advanced tumors, is known to affect both radiation sensitivity and the development of metastases [1–4]. Tumor hypoxia results from an imbalance between the supply and use of oxygen in tumor tissues. Thus, major determinants of tumor hypoxia include the structure and functionality of tumor vasculature and the degree of angiogenesis [5–8]. The direct measurement of tumor hypoxia usually requires invasive procedures such as the insertion of polarographic electrodes. However, such invasive methods are restricted both spatially and temporally, being limited to a relatively small number of measurements on easily accessible tumors at, typically, a single point in time. Noninvasive imaging offers several advantages, including the feasibility of longitudinal measurements on the same subject, the generation of complete three-dimensional maps of tumor hypoxia, and the potential application to image-guided therapy. Imaging modalities, such as magnetic resonance imaging (MRI), positron emission tomography (PET), electron paramagnetic resonance, and optical imaging, have their own unique advantages. Magnetic resonance imaging provides unique functional and structural information on tumor vasculature and physiology at high spatial resolution. Positron emission tomography can measure sensitively and quantitatively local concentrations of radioactive molecular targets of interest, such as labeled fluoromisonidazole (^{18}F-Fmiso).

^{18}F-Fmiso PET is currently under intense investigation as a method of imaging tumor hypoxia. This is based on the selective bioreduction of ^{18}F-Fmiso in hypoxic tumor regions followed by the binding of its metabolites to macromolecules [9–12]. However, the spatial resolution, based on the full-width half-maximum (FWHM) of the point spread function of the PET activity signal, is relatively coarse, ranging from 1 to 2 mm for dedicated small-animal scanners to 5 to 6 mm for clinical PET scanners. Magnetic resonance techniques provide unique opportunities to obtain noninvasive structural and functional information on tumor vasculature and physiology with anatomical details at finer spatial resolution. Magnetic resonance methods, which include dynamic contrast-enhanced MRI (DCE-MRI) [13,14], blood oxygen level–dependent imaging [15], fluorine-19 MR measurements of oxygen-sensitive compounds [16–18], and the measurement of lactate [19,20], may provide high-spatial resolution functional information to complement other imaging modalities.

In particular, DCE-MRI provides vasculature/perfusion information of the tumor microenvironment [21,22] and, thus, not only offers complementary information to PET hypoxia imaging but also may address the relationship between tumor hypoxia and vasculature. In this article, we focus on the relationship between DCE-MRI studies using Gd-DTPA as the contrast agent, and dynamic ^{18}F-Fmiso PET, in the syngeneic Dunning R3327-AT prostate tumor in rats. The *in vivo* imaging results were validated by *ex vivo* studies featuring staining with hematoxylin/eosin (H&E) (tumor necrosis) and pimonidazole (tumor hypoxia) together with ^{18}F digital autoradiography (DAR; ^{18}F-Fmiso distribution) on tumor tissue sections accurately registered to the corresponding *in vivo* slices. Accurate registration of macroscopic (MRI and PET) and microscopic images (H&E, pimonidazole and ^{18}F DAR) is a unique and important feature of the current study.

Experimental Methods

Animal Preparation

Animal studies were conducted in compliance with protocols approved by the Institutional Animal Care and Use Committee of Memorial Sloan-Kettering Cancer Center (MSKCC). The rat prostate cancer cell line R3327-AT [23] was cultured in Dulbecco's modified Eagle's medium supplemented with 10% fetal calf serum, 100 U/ml penicillin, and 100 μg/ml streptomycin at 37°C in a humidified CO_2 incubator. Cells were harvested on reaching 75% to 80% confluence and suspended in phosphate-buffered saline (PBS) at a final concentration of 2×10^6 cells/0.1 ml. Two to four million R3327-AT cells were injected in the right hind leg of 6- to 8-week-old Copenhagen rats. Tumor volume (V) was calculated as $V = (\pi/6) \times x \times y \times z$, where x, y, and z were the three orthogonal dimensions of the tumor [24]. The experiments were performed over a tumor size range of 500–2500 mm^3. A total of six rats were used. At the start of each experiment, the tail vein was catheterized with a 24G catheter and connected to a three-way stopcock (Stopcock Nylon 3-Way, 420163-4503; Kimble Kontes LLC, NJ), facilitating intravenous (IV) injection of the different agents at various stages of the multimodality imaging experiment. The catheter was kept patent by injecting heparinized saline.

Magnetic Resonance Coil and Fiduciary Marker Assembly

The MRI coil [diameter (D) = 4 cm, Helmholtz configuration] was constructed in two parts (Figure 1*A*) with the upper part of the MRI coil and marker assembly initially detached to facilitate subsequent positioning of the animal. The spatial marker assembly is shown in Figure 1*A* attached to the rest of coil-marker system, and Figure 1*B* shows an enlarged side view of the marker assembly alone (adapted from [25,26]). The marker assembly was composed of two cylindrical disks and one flat plate. The top disk, referred to as the marker holder disk [D = 1.5 cm, thickness (t) = 0.9 cm] had three holes (D = 0.9 mm) for the vertical markers. A bottom histology marker disk (D = 1.5 cm, t = 0.5 cm) with identically aligned holes was separated from the marker holder disk by a flat plate. Separate release screws fastened each disk to the flat plate, which was fixed to the top of the radiofrequency coil. At the end of the imaging experiments, the histology marker disk was detached from the rest of the marker assembly and served as a reference to align the tumor sections with the *in vivo* image slices as described below (procedure detailed in the Preparation of Tumor Cryosections section). The flat plate had one side hole to contain a horizontal marker. An additional holder was placed at the center of the bottom coil with a grooved disk (D = 1 cm, t = 0.3 cm) containing another horizontal marker as shown in Figure 1*A*. The three vertical (forming an oblique triangle with lengths of 0.9, 0.7, and 0.5 cm, respectively) and two leveled horizontal markers (22G catheter; Terumo Surflo I.V. Catheter, Somerset, NJ) were filled with Gd-DTPA–doped and red-colored water, sealed at the ends with Critoseal (Cascade Healthcare, Portland, OR), and placed at each of the designated positions in the marker holders. The three vertical markers were pushed into the 0.9-mm-sized holes through the two separate cylindrical disks (the marker holder and histology marker disks). The three vertical and two horizontal markers appear as the red tubes in Figure 1*A*. The distance between the top and bottom coil was adjustable over a range of 2 to 3 cm to accommodate tumors of various sizes.

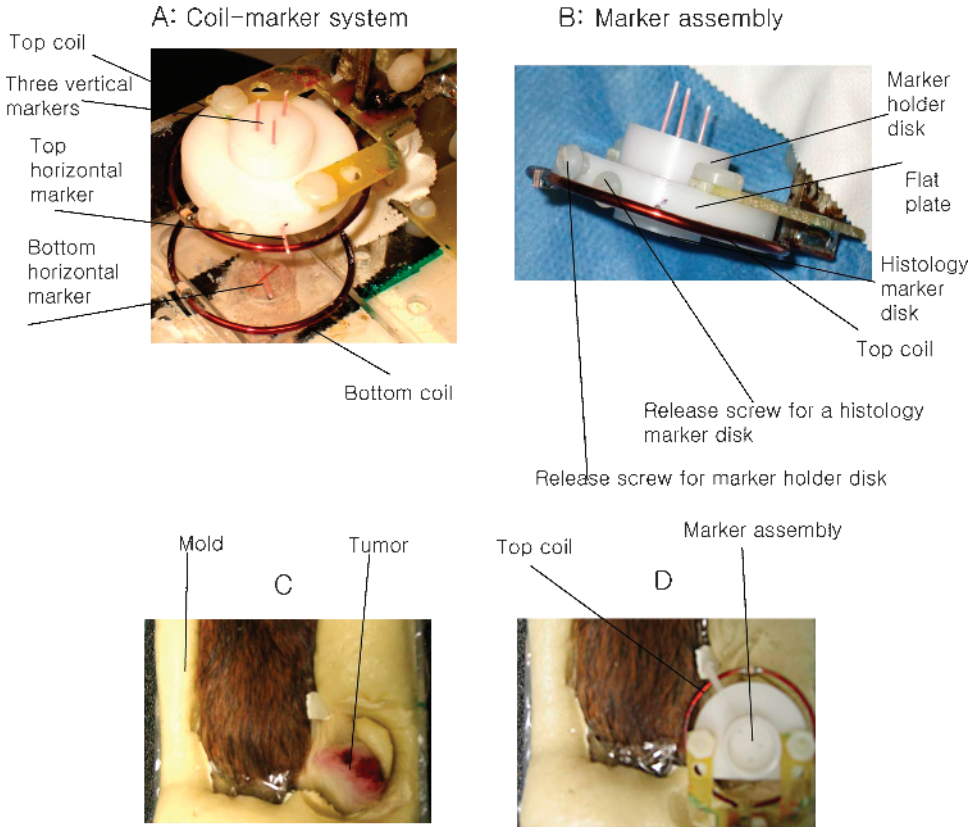

Figure 1. Photographs illustrating animal positioning and molding process on the home-built MR/PET animal holder with stereotactic marker system. (A) An enlarged picture of the stereotactic coil-marker system for MR/PET with actual markers (22G catheter, appearing as red tubes) placed in position. (B) Side view of the marker holder and histology disk. The tumor without (C) and with marker assembly in place (D) is shown after securing the animal on the holder. The release screws for vertical marker holder and histology disk were used to disengage each piece independently.

Animal Immobilization

The animal was placed on a plexiglass holder, and a rapidly setting mold was formed to keep it in place on the plastic wrap–lined animal holder with a respiration monitor pad (SA Instruments, Inc., Stony Brook, NY) placed under the animal's abdomen. The animal was anesthetized with isoflurane (1%-2%), lined in plastic wrap, and placed prone on the holder with its tumor-bearing hind leg outstretched above the bottom part of the MR coil (Figure 1*C*). The animal-positioning mold was made by mixing SecureFoam foaming reagents (Bionix Radiation Therapy, Toledo, OH) "A" and "B" (15 g each) together and pouring them on the plexiglass holder lateral to the animal [27], effectively immobilizing the animal and its leg. After allowing 5 to 7 minutes for the mold to cure, the top part of the MRI coil including the marker assembly was attached back to the circuitry and placed on the top of tumor (Figure 1*D*).

Dynamic Contrast-Enhanced MRI

The DCE-MRI experiments were performed on a Bruker 7T BioSpin (Bruker, Germany) imaging spectrometer. A syringe filled with the contrast agent Gd-DTPA (0.2 mM Gd/kg, Magnevist; Berlex Laboratories, Inc., Wayne, NJ) was connected to the three-way stopcock through Gd-DTPA–filled tubing (Masterflex Norprene tubing, 6402-13). The entire assembly including the anesthetized animal was positioned inside the magnet using a spirit level and the axial MR profile. Respiration was monitored during the MR experiment. Warm air flowed through the magnet's bore to maintain the animal's temperature under isoflurane anesthesia. The MRI coil was tuned and matched to the proton frequency, followed by shimming of the sample. The coronal slices of interest were determined from a pilot scan. Spin density images [fast low-angle shot MRI, repetition interval (TR) = 500 milliseconds, echo time (TE) = 3.1 milliseconds, number of repetitions (NR) = 1, number of averages (NA) = 1, slice thickness (ST) = 0.79 mm, field of view (FOV) = 3.5 cm × 3.5 cm, matrix = 128 × 128, number of slices = 64, flip angle = 30°] were acquired to encompass the MRI marker and tumor for subsequent image registration with PET and histology. T_2-weighted MR images (rapid acquisition with refocused echoes, TR = 2000 milliseconds, TE = 30 milliseconds, NR = 1, NA = 1, ST = 0.79 mm, number of slices = 4, FOV = 3.5 cm × 3.5 cm, matrix = 128 × 128) were acquired for four tumor slices to visualize clearly the boundary between tumor and muscle. T_1-weighted DCE-MRI (fast low-angle shots, TR = 33 milliseconds, TE = 3.1 milliseconds, NR = 256, NA = 1, ST = 0.79 mm, number of slices = 4, FOV = 3.5 cm × 3.5 cm, matrix = 128 × 128, flip angle = 30°) was performed at 5.47 seconds of temporal resolution with an in-plane resolution of 273 μm × 273 μm in plane. The contrast agent Gd-DTPA was injected through the tail vein after 2 minutes of baseline acquisition followed by 20 minutes of dynamic acquisition. After the DCE-MRI studies, additional proton spin density images were reacquired and compared with the previous images to ensure that the tumors were in the identical position with respect to the marker system before and after

the DCE-MRI study. The tubing and syringe for the administration of the contrast agent Gd-DTPA were replaced by a syringe filled with pimonidazole (Hypoxyprobe, NPI, Inc., Burlington, MA). The still anesthetized animal in the holder was transported under anesthesia to the microPET facility on a mobile anesthesia cart. We have previously shown that this procedure prevents the displacement of the tumor with respect to the marker assembly [26].

Dynamic microPET

Fluorine-18-Fmiso was produced by the Radiochemistry Service at MSKCC on an EBCO TR 19/9 cyclotron (EDCO Technologies, Vancouver, Canada) as reported previously [28]. For PET studies, the MRI markers were replaced with catheter tubings filled with ^{18}F-Fmiso diluted with red dye to an activity of ~10 μCi/ml. The animal was positioned with its tumor centered in the gantry of the microPET Focus 120 (CTI Molecular Imaging, Inc., Knoxville, TN) and the animal bed horizontally aligned with respect to the MRI plane. An initial 2-minute static acquisition was performed to acquire the diluted ^{18}F-Fmiso marker images for image coregistration before the injection of the ^{18}F-Fmiso and dynamic imaging. Thus, the relatively high-activity (~1.5 mCi) ^{18}F-Fmiso injected for the dynamic imaging did not distort the images of the marker and the low-activity markers had no effect on the dynamic ^{18}F-Fmiso imaging. The injection of ^{18}F-Fmiso (~1.5 mCi) through one port of the three-way stopcock was immediately followed by the injection of pimonidazole (60 mg/kg) through another port of the stopcock. Dynamic PET scanning was initiated immediately before the injection of the ^{18}F-Fmiso and continued for 2 to 3 hours. Figure 2*A* shows a "control" dynamic PET time-activity curve of one vertical marker demonstrating the stability of the PET acquisition. The list mode data were acquired using an energy window of 350 to 750 keV and a coincidence timing window of 6 nanoseconds and were reconstructed in a three-dimensional image matrix with voxel dimensions of 0.86 mm × 0.86 mm × 0.79 mm.

Preparation of Tumor Cryosections

After the PET scan, the animal assembly was removed from the scanner and the PET markers were removed by releasing the vertical marker holder disk (previously described in the Animal Preparation section) from the coil-marker assembly while keeping the histology disk with its identical pattern of holes in place on the tumor. The animal was then euthanized in place by isoflurane overdose, and immediately after sacrifice, three catheters with steel needles were pushed through the histology marker disk into the tumor. The resulting catheter histology disk-tumor assembly ensured the coregistration of tissue sections with the *in vivo* MR and PET images. After the insertion of the catheter and needles, the bottom histology marker disk was released from the coil-marker assembly, and the animal was removed from the holder for tumor excision. The tumor was excised with the catheter histology disk-tumor assembly intact, washed once in PBS, placed into OCT (Tissue-Tek O.C.T. Compound, Sakura Finetek U.S.A., Inc., Torrance, CA) and frozen in dry ice. After the catheter histology disk-tumor assembly was frozen, the steel needles were removed leaving the catheter tubing in place. To properly orient the tissue section plane with respect to the MRI/PET imaging plane, the histology disk was oriented parallel to the cutting surface of the tumor while freezing in dry ice. The frozen tissues were stored at −80°C until later processing.

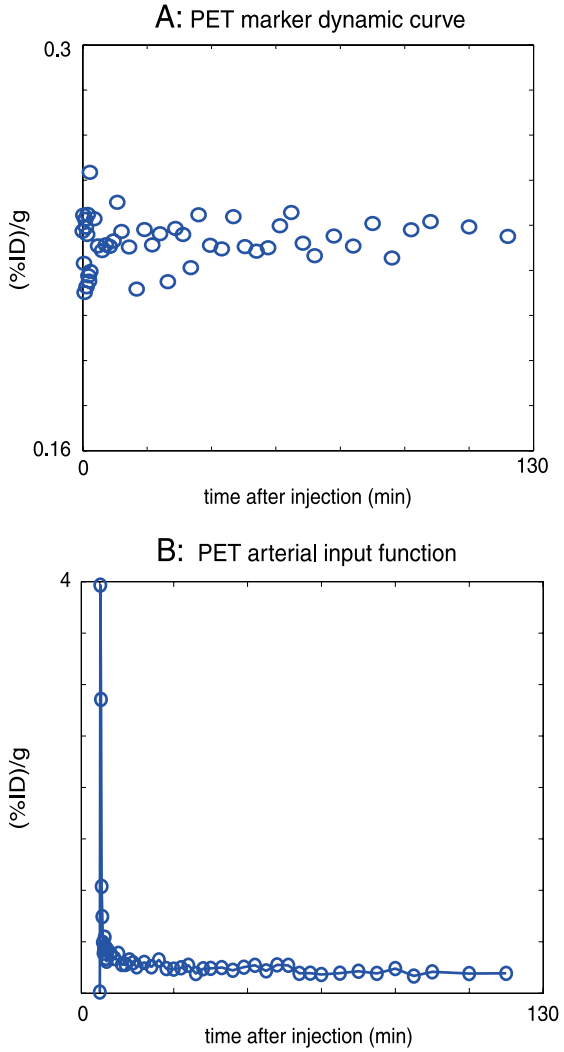

Figure 2. (A) The PET signal of one of the vertical markers for the duration of the PET measurement demonstrating the stability of the PET acquisition; the greater dispersion of points at earlier times after injection reflects the corresponding shorter time frames and lower count statistics. (B) The AIF of PET sampled from the tail region of a rat. This AIF was used for the compartment modeling of the dynamic PET time-activity curves reducing the open parameters to be fitted to four. ID indicates injected dose.

Autoradiography, Immunofluorescence, and Histology

The frozen OCT-embedded tumors were sectioned on a Microm HM500 cryostat microtome (Microm International GmbH, Walldorf, Germany). Sets of contiguous 8-μm-thick sections were cut at 0.79-mm increments across the tumor to ensure that the histology slices were sampled at positions corresponding to mid slice of the MRI and PET tomograms. To acquire the distribution of ^{18}F-Fmiso on a selected tumor, one section from each set was placed onto an imaging phosphor plate for DAR. Twenty-four hours later, the DAR images were read out in a 50-μm-pixel-size mode using a Fujifilm BAS-1800 II phosphor plate reader (Fuji Photo Film Co. Ltd., Tokyo, Japan). After autoradiography, sections were fixed in 4% paraformaldehyde solution for 10 minutes at room temperature and then blocked in SuperBlock-PBS (Pierce Biotechnology, Inc., Rockford, IL) for 1 hour. The pimonidazole distribution was detected by incubating with an antipimonidazole monoclonal antibody conjugated to fluorescein isothiocyanate (Chemicon,

Temecula, CA), diluted 1:10 in SuperBlock. Images of stained tumor sections were acquired at a high magnification (×100) using an Olympus BX40 fluorescence microscope (Olympus America Inc., Melville, NY) equipped with a motorized stage (Prior Scientific Instruments Ltd., Cambridge, UK) and an appropriate filter. The individually captured image frames were rendered into a montage of the entire tumor section (0.85 μm × 0.85 μm per pixel) using ImagePro software (Media Cybernetics Inc, Bethesda, MD). The sections were then stained with H&E for the identification of tumor necrosis and were imaged by light microscopy (0.85 μm × 0.85 μm per pixel). An image mask was generated based on the pimonidazole-stained section to distinguish the hypoxic from the nonhypoxic areas in the tumor. To reproducibly generate masks of positive pimonidazole staining, the images were converted to black and white, and a threshold for the intensity of pimonidazole background staining was obtained by measuring the average intensity of staining in the necrotic region of the tumor. The necrotic tumor region was determined from the corresponding H&E stained section. The resulting mask of positive pimonidazole staining was applied to the slope map of the late ^{18}F-Fmiso PET images to separate values corresponding to hypoxic tumor regions from those corresponding to nonhypoxic tumor regions. For viable tumor regions, a similar mask was generated from the H&E image and applied to the corresponding DCE Akep map to distinguish values of viable tumor tissue from those of necrosis.

Data Analysis

Dynamic Contrast-Enhanced MRI Analysis

The DCE-MRI data analysis was performed using in-house written Matlab (The MathWorks, Inc., Natick, MA) scripts. Dynamic signal intensity curves were obtained from the T_1-weighted signal intensity of each voxel in the dynamic MR images of the tumor slices after Gd-DTPA administration. The experimental dynamic build-up curves for each voxel in the MR images were normalized to the baseline signal and fitted using the model developed by Hoffman et al. [29] for each slice. This model is based on the linear relationship between measured saturation recovery MR signal and the concentration of Gd-DTPA in the tissue. An amplitude (*A*), which reflects the degree of relative MR signal enhancement and an exchange rate (kep), which characterizes the velocity of MR signal increase, can be derived from the two-compartment model. Consequently, the value of Akep is analogous to the slope of time-dependent MR signal enhancement and is considered an approximate measure of blood flow/perfusion of the tumor tissue [29]. The Hoffman model was used to estimate Akep values of individual voxels from the dynamic build up curves, and Akep maps were generated for the corresponding tumor slices.

Dynamic PET Analysis

List mode data were sorted into two-dimensional histograms by Fourier rebinning using a span of 3 and a maximum ring difference of 47. Images were reconstructed by filtered back-projection using a ramp filter with the Nyquist frequency as the cutoff frequency in a 128 × 128 × 95 matrix. The image data were corrected for nonuniformity of scanner response with cylinder source-based normalization, a global correction for dead-time count losses based on the singles count rate and physical decay to the time of injection. The count rates in the reconstructed images were converted to activity concentration (% of injected dose per gram of tissue, %ID/g) using a system calibration factor derived from a rat-size cylindrical phantom measurement containing a known activity concentration in aqueous ^{18}F solution. The phantom measurement also revealed that no attenuation or scatter correction was necessary. Voxel-based analysis of reconstructed dynamic PET images was performed using in-house written Matlab scripts. Kinetic curves of ^{18}F-Fmiso intensity for individual voxels for each acquired tomographic slice through the tumor (0.86 mm × 0.86 mm × 0.79 mm, 45-49 time frames during the 2~3 hours of total acquisition time) were obtained. The initial ^{18}F-Fmiso uptake into the tumor was evaluated for each animal from the first 5 minutes of the dynamic PET scan. This analysis is based on the hypothesis that the initial distribution of ^{18}F-Fmiso is mainly driven by tumor perfusion, so that the early uptake of ^{18}F-Fmiso is representative of tumor vasculature and perfusion. The later ^{18}F-Fmiso uptake was analyzed for each animal by fitting the linear slope of the last 1 hour of data from the PET time-activity curve. The analysis of the later ^{18}F-Fmiso uptake data was based on the hypothesis that the accumulation of ^{18}F-Fmiso in the hypoxic region results in a positive slope at later time after injection, whereas a well-perfused, normoxic tumor region exhibits dynamic curves with a high initial uptake followed by washout and necrotic areas display little to no initial uptake with only gradual subsequent uptake. Thus, we hypothesized that the positive slope of later time points in the dynamic PET curve of a voxel identifies areas of tumor hypoxia. The validity of this hypothesis will be demonstrated in the Experimental Results section. To quantify perfusion and tumor hypoxia, the foregoing analysis of the PET data was complemented by compartment modeling of the dynamic PET signal. The model of Thorwarth et al. [30] describes the tissue as consisting of a diffusive and an accumulative compartment based on a kinetic model with four variables fitting the experimental kinetic curves for each voxel. This model is used to extract the grade of perfusion, w0 (weighting factor of vascularized region), and the extent of hypoxia, wa × k3 (where wa is the number of viable hypoxic cells and k3 is the modified ^{18}F-Fmiso accumulation rate constant, i.e., mean degree of hypoxia), respectively [30]. The grade of perfusion and the extent of hypoxia thus identified were then compared directly with the initial uptake and later slope maps, respectively, of the ^{18}F-Fmiso time-activity curve. The arterial input function (AIF) for the ^{18}F-Fmiso compartment modeling was derived by region of interest analysis over a central blood vessel in the dynamic PET (Figure 2*B*).

Image Coregistration

Magnetic resonance and PET images were coregistered using a rigid transform derived from the three-dimensional marker systems as shown in stacked MR slices in Figure 3*A*. The slice thickness of the MR images was chosen to match the nominal slice thickness of 0.79 mm of the PET image slices, facilitating the alignment of the MR with the PET image. The maximum error for this slice coregistration can be estimated as follows. Considering that the inner diameter of a 22G catheter (MR marker) was 0.6 mm and the slice thickness was 0.79 mm, a maximum error of ±0.1 mm can occur if the marker is located off center in the slice. (Note that the MR slice for the top horizontal marker was chosen in such a way that the MR signal from the marker was confined to one slice and no detectable MR signal from adjacent slices was observed.) For the PET markers, the worst case error would occur if the center of the catheter (PET marker) were located just between two adjacent PET slices, resulting in a maximum error of ±0.4 mm. After matching the slices, the MR and PET images were aligned in plane, using the three vertical marker images of both MR and PET images. Owing to

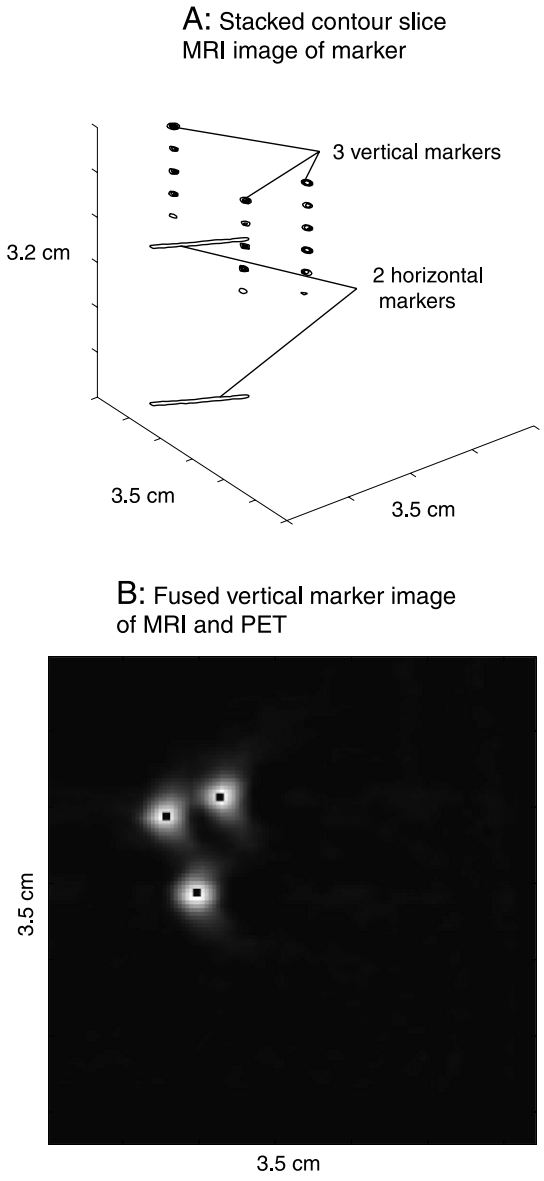

Figure 3. (A) Representative stacked two-dimensional slice images of MR markers are shown. Tumors grown on hind legs of rats are placed between the two horizontal markers. (B) The aligned MR and PET images of the three vertical markers are shown. The black center demarks the MR marker signal overlaying the coarser marker signal of the PET acquisition.

the different in-plane resolutions of PET and MR, PET marker images were interpolated to match the in-plane resolution of the MR voxel using nearest-neighbor interpolation followed by the calculation of the maximum correlation coefficient for the two images with varying translational and rotational shift of the PET marker images. The resulting optimized rotational and translational shifts were then applied to the tumor slices thereby aligning the MR and PET images (Figure 3*B*).

Experimental Results

Figure 4, *A* and *B*, shows the DCE-MRI time-signal curves and ^{18}F-Fmiso PET time-activity curves for a representative voxel from perfused, hypoxic, and necrotic regions of a tumor, respectively. The voxel for the perfused area was chosen from the high-intensity region of the DCE-MRI Akep map as shown in Figure 4*C* and the voxel representing the hypoxic region was selected from the area staining strongly for pimonidazole (Figure 4*D*) as well as from the parametric images of PET ^{18}F-Fmiso late slope maps as shown Figure 4*E*. The voxel representing tumor necrosis was chosen from the H&E-stained sections (Figure 4*F*). In the DCE-MR study, the T_1-weighted proton signal increased fastest in the nonnecrotic area as a result of rapid Gd-DTPA uptake in the well-perfused region followed by rapid washout. In contrast, hypoxic regions, typically characterized by reduced vascularization, showed a delayed Gd-DTPA uptake corresponding to a delay in signal build-up and also to a delay in washout (Figure 4*A*). In necrotic regions of the tumor, the time-dependent increase in the MR signal was slowest, and no washout could be observed for the duration of the MR experiment. In ^{18}F-Fmiso PET studies, well-perfused areas of the tumor were likewise characterized by a rapid initial increase of ^{18}F-Fmiso activity, which subsequently decreased at later times. Hypoxic areas of the tumor demonstrated lower initial activity than well-perfused areas of the tumor but continued to accumulate further ^{18}F-Fmiso during the time course of the experiment, as manifested by the distinctive positive slope (Figure 4*B*). Consequently, there was a point (~1 hour for this tumor) of crossover between the decreasing intensity of ^{18}F-Fmiso activity in well-perfused area and increasing intensity in hypoxic areas. The existence of this crossover behavior illustrated that a single static activity image at a late time point after ^{18}F-Fmiso injection may not reliably identify hypoxia because it may reflect ^{18}F-Fmiso activity in well-perfused areas that has not completely washed out. Necrotic regions of the tumor showed the least activity during the time course of the PET experiment; however, some activity is still observed. These observations agree with the hypothesis that the initial uptake of ^{18}F-Fmiso is mainly dependent on tumor vasculature and perfusion. The accumulation of ^{18}F-Fmiso activity in hypoxic regions exhibits a characteristic positive slope at later times, providing a signature for hypoxic regions without the need for complex modeling analyses. Also, as expected, necrotic areas show very low initial uptake of activity and a persisting low signal level.

Figure 5 compares early uptake (A) and later slope (C) of the ^{18}F-Fmiso time-activity curve with the compartment model parameters w0 (the grade of perfusion, Figure 5*B*) and wa × k3 (the extent of hypoxia, Figure 5*D*), respectively [30]. Tumor perfusion was well represented by the early uptake of ^{18}F-Fmiso, as well as w0, with both parameters being closely related (Figure 5*E*, Pearson's correlation with $R \sim 0.8$, $P < .001$). There was also a strong correlation between the late slope of the ^{18}F-Fmiso time-activity curve and the model-derived parameter wa × k3 (Figure 5*F*, Pearson's correlation with $R \sim 0.75$, $P < .001$). With the five open parameters in the PET compartment model, with one of them estimated by the measured AIF, caution needs to be exercised to obtain physiologically relevant values for each parameter. This is particularly problematic in severely hypoxic and necrotic tumor regions for which the signal-to-noise ratio is relatively low. In such cases, the early uptake rate and the late slope of the time-activity curves may provide similar, yet more robust measures of the respective tumor microenvironments as the latter parameters involve fewer degrees of freedom in the fitting procedure than the compartmental modeling.

In Figure 5, *G–I*, respectively, a ^{18}F digital autoradiogram (DAR), pimonidazole- and H&E-stained tissue section, and the corresponding *in vivo* MRI and ^{18}F-Fmiso PET tumor images are shown. The spatial congruence between the late (3 hours) static PET image (Figure 5*J*) and the activity distribution in the ^{18}F-autoradiogram

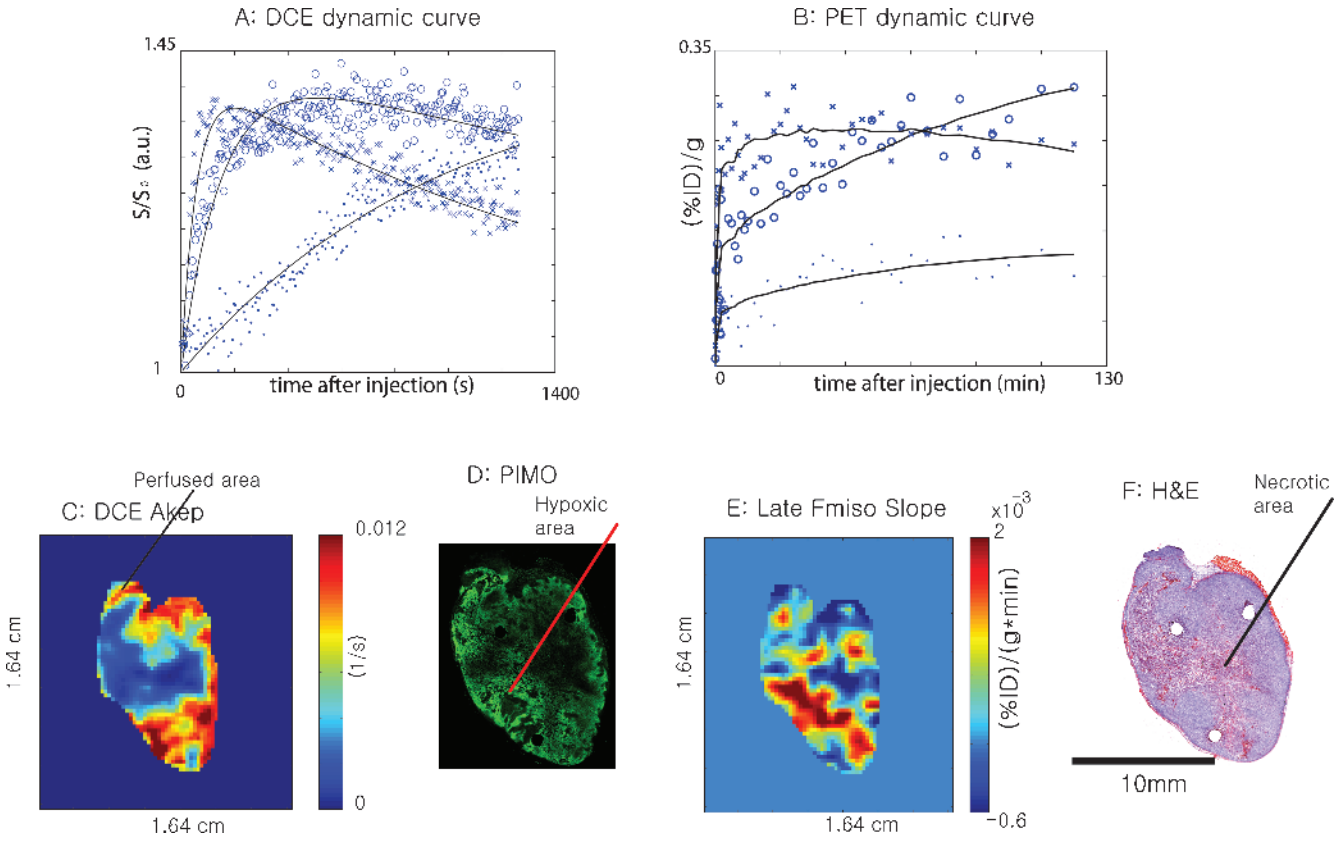

Figure 4. Characteristic dynamic uptake curves of Gd-DTPA–assisted DCE-MRI (A) and ^{18}F-Fmiso PET (B) for different tumor microenvironments (×, perfused area; ○, hypoxic area; •, necrotic area). Perfused, necrotic, and hypoxic areas were independently selected from DCE-MRI (C), H&E (F), pimonidazole (D) and late Fmiso slope (E) images, respectively, and corresponding dynamic curves are plotted in A and B.

(Figure 5*G*) is visually apparent. However, the 3-hour static image of PET (Figure 5*J*) does not show the hot rim present in the DAR image. Considering the fact that the static image of the late PET scan and the DAR have grossly different (~40-fold) resolution, the voxel-averaging effect of PET needs to be taken into account to understand this discrepancy (see the Discussion section). It is also important to note the apparent discrepancy between the significant rim activity of ^{18}F-Fmiso in the DAR and the apparent lack of pimonidazole positivity in this region. Given the likelihood that the rim of this slice is well perfused, as may be inferred from the Akep map (Figure 5*K*), we hypothesize that the high-intensity region of ^{18}F-Fmiso around the tumor rim in the tissue section contains radioactivity that did not fully wash-out from the perfused area (see the Discussion section). In principle, the late slope map of ^{18}F-Fmiso (Figure 5*C*), or the wa × k3 parametric map from compartment modeling (Figure 5*D*) should eliminate false-positive hypoxic regions such as this; however, in this particular case, the issue is complicated by the voxel-averaging effect. Overall, the spatial congruence of the pimonidazole-stained section, the late ^{18}F-Fmiso slope map (Figure 5*C*), and the wa × k3 parametric map from compartment modeling (Figure 5*D*) suggests that the dynamic acquisition of ^{18}F-Fmiso PET provides a more reliable way of identifying regions of hypoxia than a late static ^{18}F-Fmiso image.

In Figure 6, the relationship between Akep map (A) and early ^{18}F-Fmiso uptake values (B) and late ^{18}F-Fmiso slope (C) for tumors of varying sizes are shown. Small tumors (~500 mm^3) were uniformly well perfused, as could be seen in both, the DCE Akep maps (Figure 6*A-1*) and early ^{18}F-Fmiso uptake PET images (Figure 6*B-1*). The corresponding voxel-by-voxel scatterplots were rather concentrated at higher values over a small dynamic range (Figure 6*D-1*) and show a weak positive correlation between DCE Akep and early ^{18}F-Fmiso uptake (R ~ 0.2). Intermediate-sized tumors (500 to ~1200 mm^3; Figure 6, *A-2* and *A-3*) were well perfused around the rim of the tumor with high DCE Akep values and high early PET uptake values (Figure 6, *B-2* and *B-3*). The voxel-by-voxel scatterplot demonstrated higher positive correlations (R = 0.5~0.7; Figure 6, *D-2* and *D-3*) with values distributed over a larger dynamic range than for the smaller well-perfused tumors. For large tumors (>1500 mm^3; Figure 6*A-4*), the necrotic portion appears to be dominant, and the positive correlation between DCE Akep values and early ^{18}F-Fmiso PET values is again poorer (R ~ 0.3; Figure 6*D-4*). These features can be understood in terms of the development of hypoxic and necrotic regions as the tumor grows, which is true for the R3327-AT tumor model used in this study [31,32].

The direct spatial relationship between flow/perfusion as represented by DCE-MRI Akep parametric maps and hypoxia as represented by late ^{18}F-Fmiso PET slope map was evaluated in their adequacy to address the fundamental relationship between tumor microvasculature and hypoxia. Small tumors (~500 mm^3; Figure 6*A-1*), which appear to be uniformly well perfused, exhibit uniformly negative values in the corresponding late ^{18}F-Fmiso slope maps (Figure 6*C-1*) and, thus, predictably, appear to be nonhypoxic. The

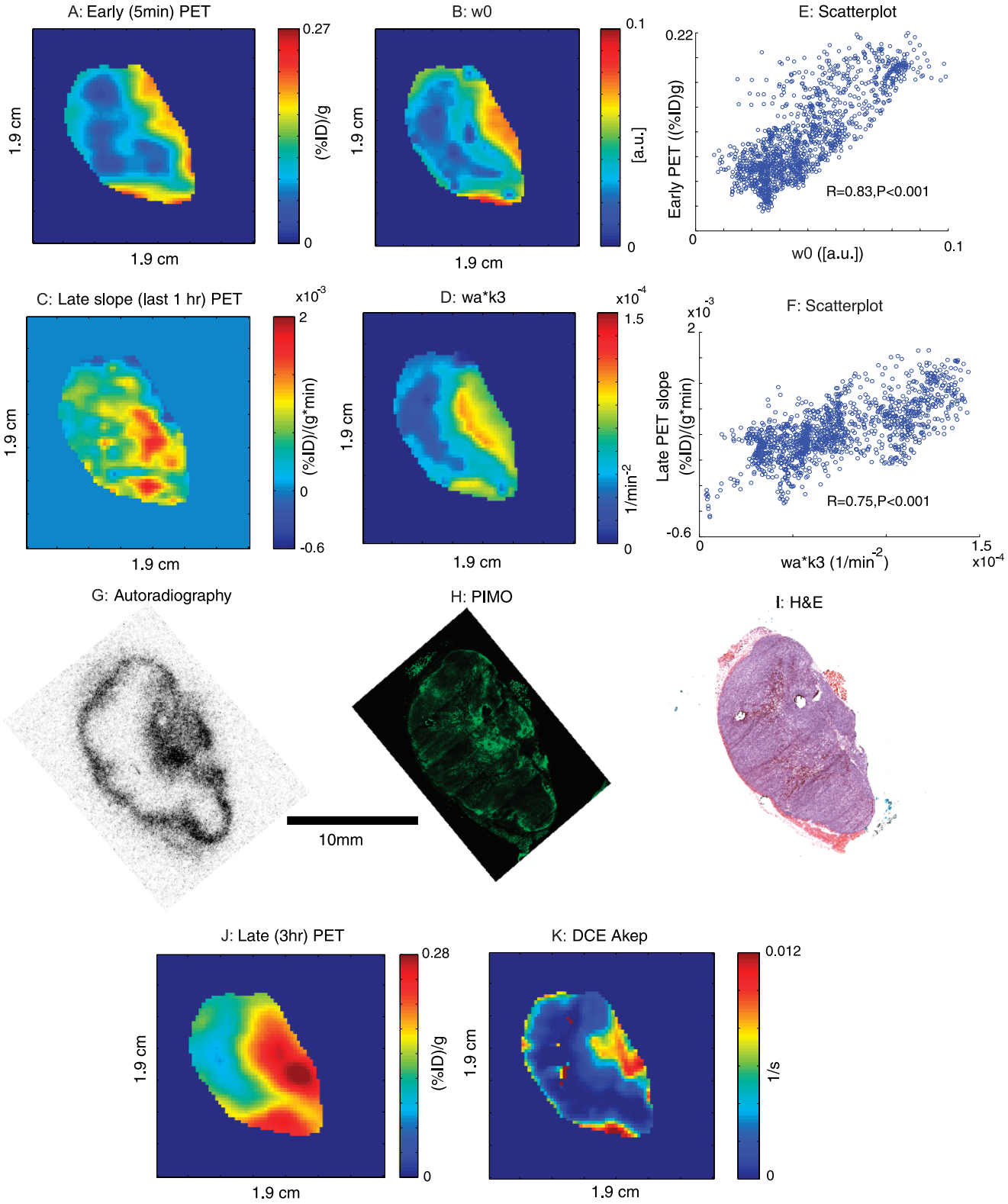

Figure 5. (A) Early (5 minutes) ^{18}F-Fmiso uptake values of representative tumor (1230 mm^3). (B) The w0 (grade of perfusion) map from the compartment modeling of the dynamic PET signal. (C) Late slope map (last 1 hour of acquisition) of later ^{18}F-Fmiso PET. (D) wa × k3 (the extent of hypoxia) map from the compartment modeling of the dynamic PET signal. (E) Scatterplot comparing voxel-by-voxel early ^{18}F-Fmiso uptake with w0. (F) Scatterplot comparing voxel-by-voxel the late slope map of ^{18}F-Fmiso PET with wa × k3. (J) A static PET intensity image at 3 hours after injection. (K) DCE Akep map. G, H, and I are ^{18}F-Fmiso autoradiography, pimonidazole staining (PIMO), and H&E staining, respectively.

voxel-by-voxel scatterplot between late ^{18}F-Fmiso slope and Akep shows a weak (R ~ −0.2) but significant (P < .001) negative correlation (Figure 6*E-1*). For intermediate-size heterogeneous tumors, the regions of positive slopes appeared mainly in the less-perfused areas, and there were stronger negative correlations (R ~ −0.35) between DCE-MRI Akep and the late slope ^{18}F-Fmiso PET curves (Figure 6, *C-2*, *C-3*, *E-2*, and *E-3*). As the size of the tumors increases beyond 1500 mm^3, no significant uptake of ^{18}F-Fmiso was observed above the

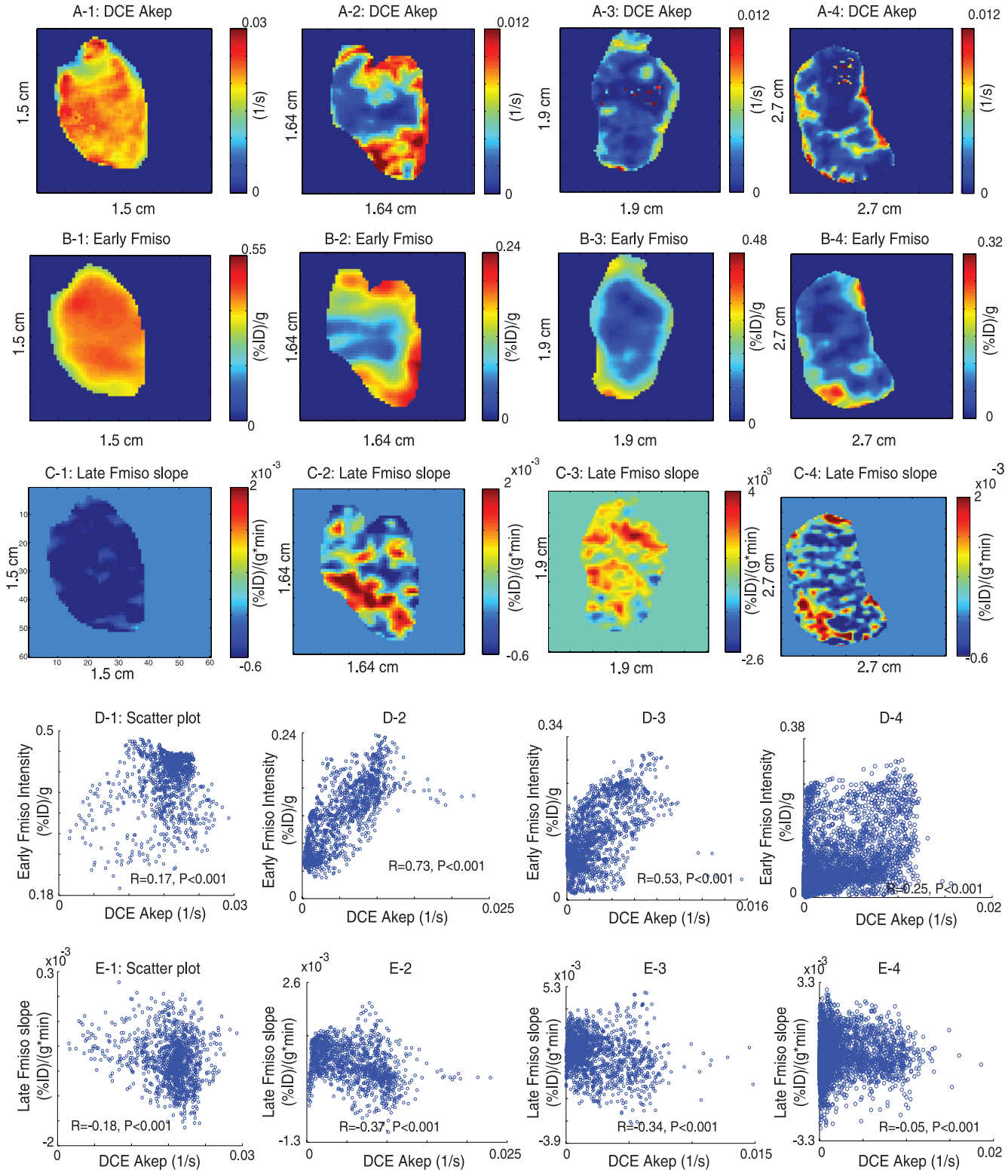

Figure 6. The rows of A, B, and C show DCE-Akep map, early (5 minutes) ^{18}F-Fmiso uptake values, and slope map of later ^{18}F-Fmiso curve for a slice from four different animals (numbered 1 to 4), respectively. The rows of D and E plot voxel-by-voxel scatterplots for the direct comparison of these quantities. The tumor sizes are 478 mm^3 (1), 744 mm^3 (2), 870 mm^3 (3), and 2531 mm^3 (4).

noise level except in some parts of the tumor rim, matching the Gd-DTPA uptake pattern for this large tumor (Figure 6, *C-4* and *E-4*).

Figure 7 and Figure W1 relate the values of DCE-MRI Akep to H&E staining for two representative tumor slices each from a different animal. The T_2-weighted MR image of the tumor slice (Figure 7*A* and Figure W1*A*) and the corresponding H&E slice (Figure 7*B* and Figure W1*B*) are shown. It was apparent in both tissue sections that higher values of Akep (Figure 7*C* and Figure W1*C*) correspond to the viable tumor and lower values of Akep match well with the necrotic area, as estimated from the corresponding H&E slice (Figure 7*B* and Figure W1*B*). For further quantification, a mask was generated based on the H&E staining to distinguish viable from necrotic tumor regions and was mapped onto the Akep map, as shown in Figure 7, *D* and *E*, and Figure W1, *D* and *E*, followed by histogram analysis. The histogram analysis (Figure 7*F* and Figure W1*F*) further confirmed the discrimination that the Akep values could achieve between viable and necrotic areas. The median Akep values for viable tumor regions were significantly higher than those of necrotic regions ($P < .001$). The amount of overlap was dependent on the individual tumor (Figure 7*F* and Figure W1*F*), suggesting that at the extreme tails of the distribution curves of the Akep values, there may be some minimal overlap between necrotic and viable tissue. However, the shapes of the histograms are markedly different allowing discrimination between viable and necrotic tissue.

Figure 8 relates the slope map of late ^{18}F-Fmiso PET uptake to regions of pimonidazole-defined hypoxia. A qualitative similarity between the staining in the pimonidazole section designating hypoxia (Figure 8*A* and Figure W2*A*) and the late ^{18}F-Fmiso slope map (Figure 8*B* and Figure W2*B*) was observed, with higher slope values generally corresponding to more intense pimonidazole staining. Pimonidazole positivity masks (see the Autoradiography, Immunofluorescence, and Histology section) were applied to the slope maps of the late ^{18}F-Fmiso PET images to distinguish values corresponding to the hypoxic tumor regions (Figure 8*C* and Figure W2*C*) *versus* nonhypoxic tumor regions (Figure 8*D* and Figure W2*D*). The overlap was considerable, but histogram analysis showed a difference in the slope values between the hypoxic and nonhypoxic areas (Figure 8*E* and Figure W2*E*). The volume-averaging effect in coarser-resolution PET images appeared to be substantial and may be largely responsible for the overlap. However, the overlap between slope values of hypoxic and nonhypoxic regions was of concern and would need to be addressed before possible future clinical use.

Discussion

Multimodality imaging, specifically, DCE-MRI and dynamic ^{18}F-Fmiso PET, was performed on the R3327-AT preclinical tumor model. Corresponding tissue sections were stained with H&E and pimonidazole to relate the noninvasive, *in vivo* MRI/PET data to

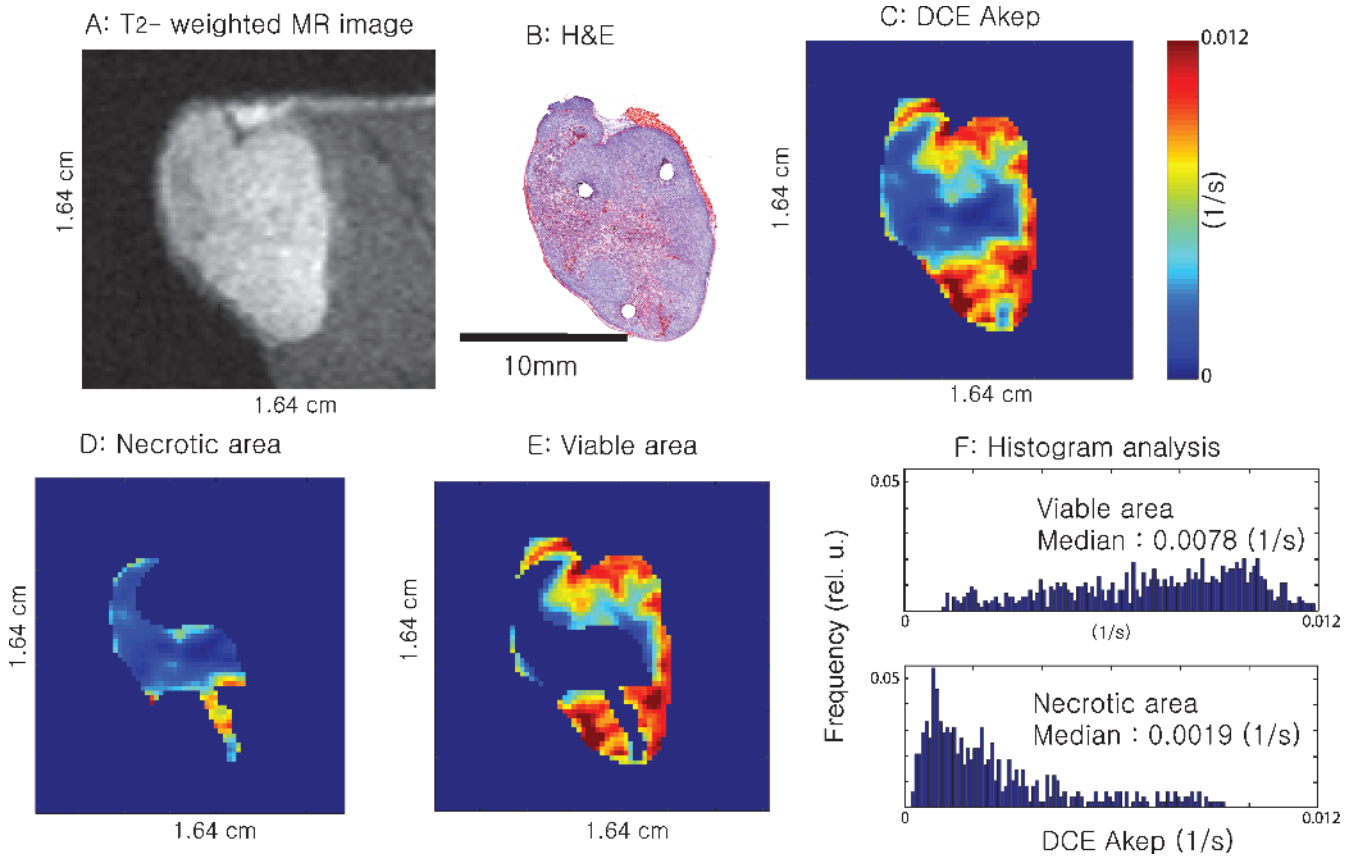

Figure 7. T_2-weighted MR image of a slice from one animal (A), corresponding H&E-stained tissue section (B), and corresponding DCE Akep map (C). D and E are the masked Akep values for the necrotic and viable tumor areas, respectively. The histograms in (F) plot the Akep values for viable and necrotic tumor areas, respectively. The median Akep values for viable tumor regions were significantly higher ($P < .001$) than those of necrotic regions. The tumor size was 744 mm^3.

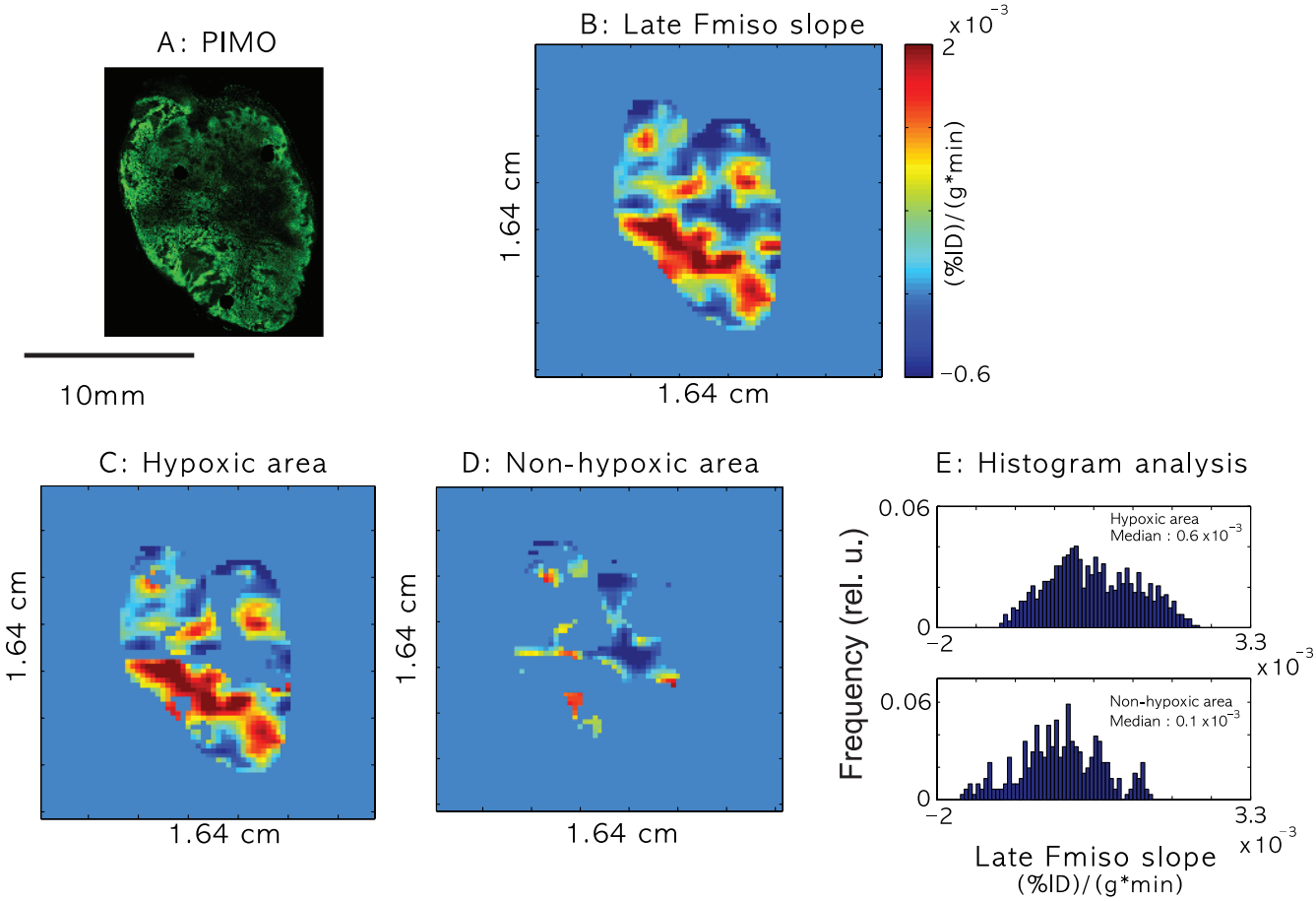

Figure 8. (A) Pimonidazole-stained (PIMO) section. (B) Late slope map of ^{18}F-Fmiso PET uptake curves. C and D are masked later ^{18}F-Fmiso PET slope values for hypoxic and nonhypoxic areas of the tumors, respectively. (E) Histogram plots of the late ^{18}F-Fmiso PET slope values for hypoxic and nonhypoxic areas of the tumors. The median values of later ^{18}F-Fmiso PET slope for hypoxic regions were significantly higher ($P < .001$) than those of nonhypoxic regions, but there was significant overlap. The tumor size was 744 mm^3.

the tumor microenvironment as determined from *ex vivo* analysis of tissue sections. The relationships between coregistered MRI and PET parameters were investigated. A perfusion-related parameter (Akep) derived from DCE-MRI yielded a positive correlation with early ^{18}F-Fmiso PET intensity and a negative correlation with late slope map of ^{18}F-Fmiso PET time-activity curve.

In vivo multimodality MRI/PET imaging of the tumor microenvironment promises many advantages for obtaining prognostic information about tumor progression or tumor response to treatment; however, caution needs to be exercised when interpreting such imaging data. Two issues, in particular, should be considered based on our experimental observations as briefly mentioned in the Experimental Results section.

Voxel-Averaging Effect in PET

Pimonidazole staining in Figure 4*D* showed significant staining on the right rim region of the tumor section adjacent to the perfused area as determined from DCE-MRI in Figure 4*C*. Conversely, the slope map derived from the dynamic PET images (Figure 4*E*) did not indicate any hypoxia in the corresponding rim region. A similar behavior was also shown for the rim of the tumor in Figure 5, where there is thin pimonidazole staining around the rim of tumor (Figure 5*H*) and a broader distribution of ^{18}F activity in the DAR (Figure 5*G*) but not in the *in vivo* PET images (Figure 5, *C*, *D*, and *J*). This effect is likely due to the volume averaging of PET resulting from its lower spatial resolution (FWHM: 2 mm) compared with other imaging modalities, particularly microscopy of tissue sections (0.85 μm × 0.85 μm per pixel at 100× magnification). This problem is exacerbated if the hypoxic region is located close to the well-perfused areas. To depict the effect of volume averaging, Gaussian blurring was applied to the original DAR (Figure 9). Figure 9*A-2* shows 40-fold blurred data, corresponding to the approximate FWHM resolution obtained from microPET imaging with no distinctive hot spots around the rim of tumor; this agrees well with the corresponding late-time (3 hours) static PET image (Figure 5*J*). Hypoxia imaging using MRI/PET is highly sensitive and specific to tumor hypoxia if the area of hypoxia is similar to the voxel size of the imaging modality used. Smaller hypoxic regions located close to necrotic or perfused tumor areas or intermittent hypoxic regions may otherwise not be detectable using these *in vivo* imaging modalities because of the voxel-averaging effect.

Perfusion Effect of ^{18}F-Fmiso Accumulation in a Tumor

It is observed that the initial uptake of ^{18}F-Fmiso is dominated by perfusion (Figures 5 and 6). It is also shown from the ^{18}F-Fmiso time-activity curve of ^{18}F-Fmiso PET that there exists a crossover point of

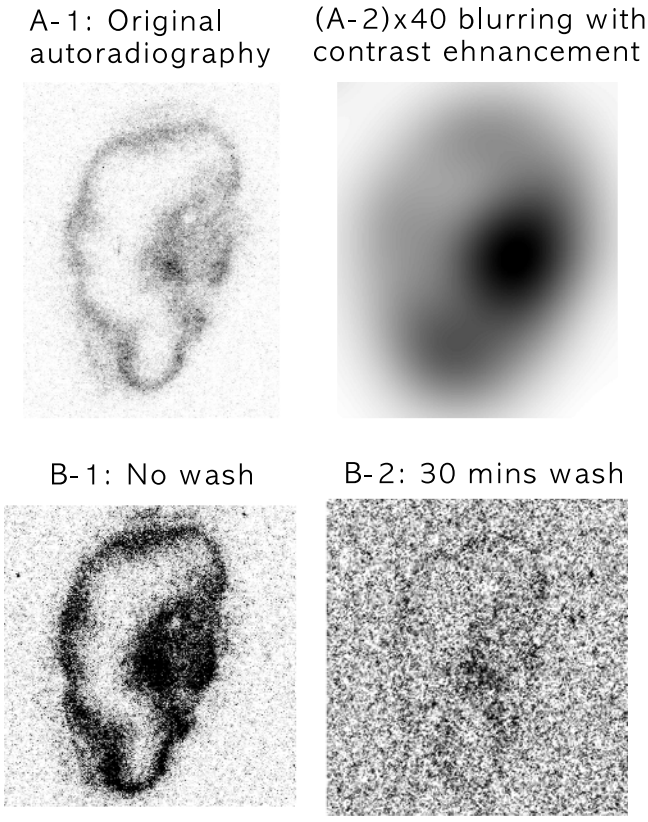

Figure 9. A-1 shows the original ^{18}F-Fmiso DAR image at 50 μm × 50 μm in-plane pixel resolution from the tumor shown in Figure 5. A-2 shows the same image with a Gaussian blur applied (radius = 40 pixels), corresponding to the approximate FWHM resolution obtained from microPET imaging (~2 mm), and with image contrast enhancement. B shows a ^{18}F-Fmiso autoradiograph obtained from a representative tumor section using the tumor shown in Figure 5 before and after a series of wash steps. B-1 shows the radionuclide distribution obtained using standard methods. B-2 shows the DAR image of the tumor section obtained after washing the section in PBS for 30 minutes, demonstrating the washout of unbound ^{18}F-Fmiso.

signal intensity between well-perfused and hypoxic areas (Figure 4*B*). Awareness of this crossover effect is critical if a static ^{18}F-Fmiso PET image is used for the detection of hypoxic regions of the tumor. Our data show that different tumors are unlikely to have similar crossover time point because the tumor microenvironment could be very different. To address the hypothesis that the high-intensity region of ^{18}F-Fmiso around the tumor rim in the tissue section contains radioactivity, which did not fully wash out from the perfused area, the tumor section was washed in PBS for 1, 5, and 30 minutes to remove any unbound ^{18}F-Fmiso and was radiographically evaluated. The images at the *bottom row* of Figure 9 depict the DARs of the frozen section (Figure 9*B-1*) and after a 30-minute wash in PBS (Figure 9*B-2*). The signal-to-noise ratio of activity drops significantly even after the first wash, and the thickness of the rim is continually reduced with each wash, eventually approaching the corresponding image of pimonidazole (Figures 5*H* and 9*B-2*). The size of the hot spot in the ^{18}F autoradiogram of the slice (Figure 9, *B-1* and *B-2*) decreased with each wash as well and closely approximates the size and location of the intense spot in the pimonidazole-stained section (Figure 5*H*) and late slope map of ^{18}F-Fmiso (Figure 5*C*). The possibility of introducing unbound ^{18}F-Fmiso during tissue sectioning cannot be fully excluded when explaining the visible hot rim in DAR, although it is considered less likely.

Also, other aspects related to the sequential acquisition of the MR and PET data in this study need to be considered. The fiduciary marker system and the molding of the animal with the tumor grown on the leg allow stable positioning of the tumor between the MR and PET acquisitions and thus coregistration of the MR and PET images using a rigid transformation. However, in a clinical setting, the tumor may be deformable and/or may be susceptible to both voluntary and involuntary (e.g., respiratory) patient motions. Thus, image coregistration would need to account for motion or tissue deformation, which is a more complex problem to solve and less robust than a rigid transformation. This could be further aggravated by significant tissue movement present between the two imaging studies and would most likely result in larger coregistration errors than can be expected in the current study. Also, performing the MR and PET acquisition sequentially assumes that the gross tumor physiology does not change between the experiments. Simultaneous acquisition of the MR and PET images would therefore be highly desirable. The recent developments of combined MR/PET systems (preclinical and clinical [33–36]), which allow such simultaneous image acquisition, will be invaluable in pursuing studies such as those presented in this article.

Previous clinical studies support the importance of measuring both tumor perfusion and hypoxia [37,38]. Bruehlmeier et al. [37] showed in a PET study of human brain tumors that the initial uptake of ^{18}F-Fmiso was perfusion-dependent, whereas late uptake was independent of perfusion. Thorwarth et al. [38] showed in a PET study of human head-and-neck cancers that hypoxia and perfusion were independent from each other but both affected radiation treatment outcome. Their data clearly illustrate the need for both perfusion and hypoxia measurements to investigate the tumor microenvironment. Although perfusion and hypoxia were found to be independent, their results emphasize the interaction of these parameters. The combined measurements of both hypoxia and perfusion were shown to be clinically predictive of outcome, whereas neither parameter alone was related to outcome. The clinical data cited support the validity and relevance of the preclinical data presented in this article because the tumor microenvironment in both preclinical and clinical studies demonstrates significant heterogeneity in perfusion and hypoxia. Thus, the potential utility of further clinical and preclinical studies to evaluate perfusion, hypoxia, and their relationship to outcome is warranted.

Bearing in mind the caveats listed above, the combination of DCE-MRI and ^{18}F-Fmiso PET could be proposed as noninvasive clinical imaging tool in the evaluation of tumor prognosis, planning for radiation therapy or chemotherapy, and monitoring of treatment response. These noninvasive imaging modalities have particular promise because they provide not only anatomically but also clinically important functional information of the tumor microenvironment.

Acknowledgments

The authors thank Valerie A. Longo and Mihai Coman for their technical assistance, H. Carl Le for helpful discussions, and Shangde Cai and Eva Burnazi for the ^{18}F-Fmiso production.

References

[1] Chaudary N and Hill RP (2006). Hypoxia and metastasis in breast cancer. *Breast Dis* **26**, 55–64.

[2] Hockel M, Schlenger K, Mitze M, Schaffer U, and Vaupel P (1996). Hypoxia and radiation response in human tumors. *Semin Radiat Oncol* **6**, 3–9.
[3] Vaupel P, Mayer A, Briest S, and Hockel M (2005). Hypoxia in breast cancer: role of blood flow, oxygen diffusion distances, and anemia in the development of oxygen depletion. *Adv Exp Med Biol* **566**, 333–342.
[4] Menon C and Fraker DL (2005). Tumor oxygenation status as a prognostic marker. *Cancer Lett* **221**, 225–235.
[5] Dachs GU and Chaplin DJ (1998). Microenvironmental control of gene expression: implications for tumor angiogenesis, progression, and metastasis. *Semin Radiat Oncol* **8**, 208–216.
[6] Secomb TW, Hsu R, Braun RD, Ross JR, Gross JF, and Dewhirst MW (1998). Theoretical simulation of oxygen transport to tumors by three-dimensional networks of microvessels. *Adv Exp Med Biol* **454**, 629–634.
[7] Haroon ZA, Peters KG, Greenberg CS, and Dewhirst MW (1998). Angiogenesis and oxygen transport in solid tumors. In BA Teicher (Ed.). *Antiangiogenic Agents in Cancer Therapy.* Totowa, NJ: Humana Press Inc., pp. 3–21.
[8] Neeman M, Provenzale JM, and Dewhirst MW (2001). Magnetic resonance imaging applications in the evaluation of tumor angiogenesis. *Semin Radiat Oncol* **11**, 70–82.
[9] Koh WJ, Rasey JS, Evans ML, Grierson JR, Lewellen TK, Graham MM, Krohn KA, and Griffin TW (1992). Imaging of hypoxia in human tumors with [F-18] fluoromisonidazole. *Int J Radiat Oncol Biol Phys* **22**, 199–212.
[10] Casciari JJ, Graham MM, and Rasey JS (1995). A modeling approach for quantifying tumor hypoxia with [F-18]fluoromisonidazole PET time-activity data. *Med Phys* **22**, 1127–1139.
[11] Serganova I, Humm J, Ling C, and Blasberg R (2006). Tumor hypoxia imaging. *Clin Cancer Res* **12**, 5260–5264.
[12] Lee ST and Scott AM (2007). Hypoxia positron emission tomography imaging with ^{18}F-fluoromisonidazole. *Semin Nucl Med* **37**, 451–461.
[13] Tofts PS (1997). Modeling tracer kinetics in dynamic Gd-DTPA MR imaging. *J Magn Reson Imaging* **7**, 91–101.
[14] Kuhl CK, Mielcareck P, Klaschik S, Leutner C, Wardelmann E, Gieseke J, and Schild HH (1999). Dynamic breast MR imaging: are signal intensity time course data useful for differential diagnosis of enhancing lesions? *Radiology* **211**, 101–110.
[15] Ogawa S, Lee TM, Kay AR, and Tank DW (1990). Brain magnetic resonance imaging with contrast dependent on blood oxygenation. *Proc Natl Acad Sci USA* **87**, 9868–9872.
[16] Sotak CH, Hees PS, Huang HN, Hung MH, Krespan CG, and Raynolds S (1993). A new perfluorocarbon for use in fluorine-19 magnetic resonance imaging and spectroscopy. *Magn Reson Med* **29**, 188–195.
[17] Procissi D, Claus F, Burgman P, Koziorowski J, Chapman JD, Thakur SB, Matei C, Ling CC, and Koutcher JA (2007). *In vivo* ^{19}F magnetic resonance spectroscopy and chemical shift imaging of tri-fluoro-nitroimidazole as a potential hypoxia reporter in solid tumors. *Clin Cancer Res* **13**, 3738–3747.
[18] Mason RP, Antich PP, Babcock EE, Constantinescu A, Peschke P, and Hahn EW (1994). Non-invasive determination of tumor oxygen tension and local variation with growth. *Int J Radiat Oncol Biol Phys* **29**, 95–103.
[19] He Q, Shungu DC, van Zijl PC, Bhujwalla ZM, and Glickson JD (1995). Single-scan *in vivo* lactate editing with complete lipid and water suppression by selective multiple-quantum-coherence transfer (Sel-MQC) with application to tumors. *J Magn Reson B* **106**, 203–211.
[20] Jue T, Arias-Mendoza F, Gonnella NC, Shulman GI, and Shulman RG (1985). A ^{1}H NMR technique for observing metabolite signals in the spectrum of perfused liver. *Proc Natl Acad Sci USA* **82**, 5246–5249.
[21] Hylton N (2006). Dynamic contrast-enhanced magnetic resonance imaging as an imaging biomarker. *J Clin Oncol* **24**, 3293–3298.
[22] Egeland TA, Gaustad JV, Benjaminsen IC, Hedalen K, Mathiesen B, and Rofstad EK (2008). Assessment of fraction of hypoxic cells in human tumor xenografts with necrotic regions by dynamic contrast-enhanced MRI. *Radiat Res* **169**, 689–699.
[23] Isaacs JT, Isaacs WB, Feitz WF, and Scheres J (1986). Establishment and characterization of seven Dunning rat prostatic cancer cell lines and their use in developing methods for predicting metastatic abilities of prostatic cancers. *Prostate* **9**, 261–281.
[24] Euhus DM, Hudd C, LaRegina MC, and Johnson FE (1986). Tumor measurement in the nude mouse. *J Surg Oncol* **31**, 229–234.
[25] Humm JL, Ballon D, Hu YC, Ruan S, Chui C, Tulipano PK, Erdi A, Koutcher J, Zakian K, Urano M, et al. (2003). A stereotactic method for the three-dimensional registration of multi-modality biologic images in animals: NMR, PET, histology, and autoradiography. *Med Phys* **30**, 2303–2314.
[26] Zhang M, Huang M, Le C, Zanzonico PB, Claus F, Kolbert KS, Martin K, Ling CC, Koutcher JA, and Humm JL (2008). Accuracy and reproducibility of tumor positioning during prolonged and multi-modality animal imaging studies. *Phys Med Biol* **53**, 5867–5882.
[27] Zanzonico P, Campa J, Polycarpe-Holman D, Forster G, Finn R, Larson S, Humm J, and Ling C (2006). Animal-specific positioning molds for registration of repeat imaging studies: comparative microPET imaging of F18-labeled fluoro-deoxyglucose and fluoro-misonidazole in rodent tumors. *Nucl Med Biol* **33**, 65–70.
[28] Engelhardt EL, Schneider RF, Seeholzer SH, Stobbe CC, and Chapman JD (2002). The synthesis and radiolabeling of 2-nitroimidazole derivatives of cyclam and their preclinical evaluation as positive markers of tumor hypoxia. *J Nucl Med* **43**, 837–850.
[29] Hoffmann U, Brix G, Knopp MV, Hess T, and Lorenz WJ (1995). Pharmacokinetic mapping of the breast: a new method for dynamic MR mammography. *Magn Reson Med* **33**, 506–514.
[30] Thorwarth D, Eschmann SM, Paulsen F, and Alber M (2005). A kinetic model for dynamic [^{18}F]-Fmiso PET data to analyse tumour hypoxia. *Phys Med Biol* **50**, 2209–2224.
[31] Thorndyke C, Meeker BE, Thomas G, Lakey WH, McPhee MS, and Chapman JD (1985). The radiation sensitivities of R3327-H and R3327-AT rat prostate adenocarcinomas. *J Urol* **134**, 191–198.
[32] Hunjan S, Zhao D, Constantinescu A, Hahn EW, Antich PP, and Mason RP (2001). Tumor oximetry: demonstration of an enhanced dynamic mapping procedure using fluorine-19 echo planar magnetic resonance imaging in the Dunning prostate R3327-AT1 rat tumor. *Int J Radiat Oncol Biol Phys* **49**, 1097–1108.
[33] Catana C, Procissi D, Wu Y, Judenhofer MS, Qi J, Pichler BJ, Jacobs RE, and Cherry SR (2008). Simultaneous *in vivo* positron emission tomography and magnetic resonance imaging. *Proc Natl Acad Sci USA* **105**, 3705–3710.
[34] Judenhofer MS, Wehrl HF, Newport DF, Catana C, Siegel SB, Becker M, Thielscher A, Kneilling M, Lichy MP, Eichner M, et al. (2008). Simultaneous PET-MRI: a new approach for functional and morphological imaging. *Nat Med* **14**, 459–465.
[35] Schlemmer HP, Pichler BJ, Krieg R, and Heiss WD (2008). An integrated MR/PET system: prospective applications. *Abdom Imaging*.
[36] Schlemmer HP, Pichler BJ, Schmand M, Burbar Z, Michel C, Ladebeck R, Jattke K, Townsend D, Nahmias C, Jacob PK, et al. (2008). Simultaneous MR/PET imaging of the human brain: feasibility study. *Radiology* **248**, 1028–1035.
[37] Bruehlmeier M, Roelcke U, Schubiger PA, and Ametamey SM (2004). Assessment of hypoxia and perfusion in human brain tumors using PET with ^{18}F-fluoromisonidazole and ^{15}O-H_2O. *J Nucl Med* **45**, 1851–1859.
[38] Thorwarth D, Eschmann SM, Scheiderbauer J, Paulsen F, and Alber M (2005). Kinetic analysis of dynamic ^{18}F-fluoromisonidazole PET correlates with radiation treatment outcome in head-and-neck cancer. *BMC Cancer* **5**, 152.

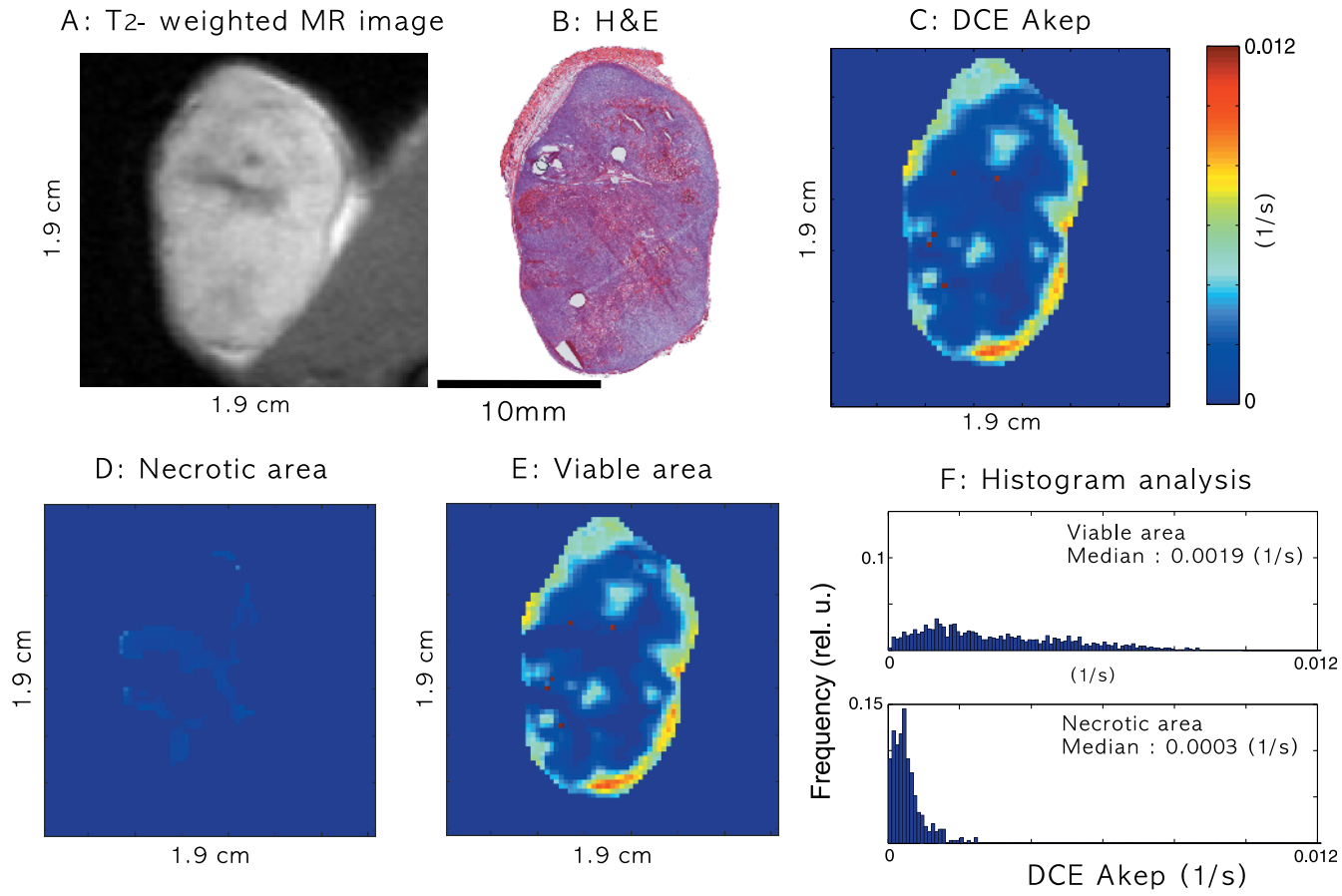

Figure W1. T_2-weighted MR image of a slice from one animal (A), corresponding H&E-stained tissue section (B), and corresponding DCE Akep map (C). D and E are the masked Akep values for the necrotic and viable tumor areas, respectively. The histograms in F plot the Akep values for viable and necrotic tumor areas, respectively. The median Akep values for viable tumor regions were significantly higher ($P < .001$) than those of necrotic regions. The tumor size was 870 mm^3.

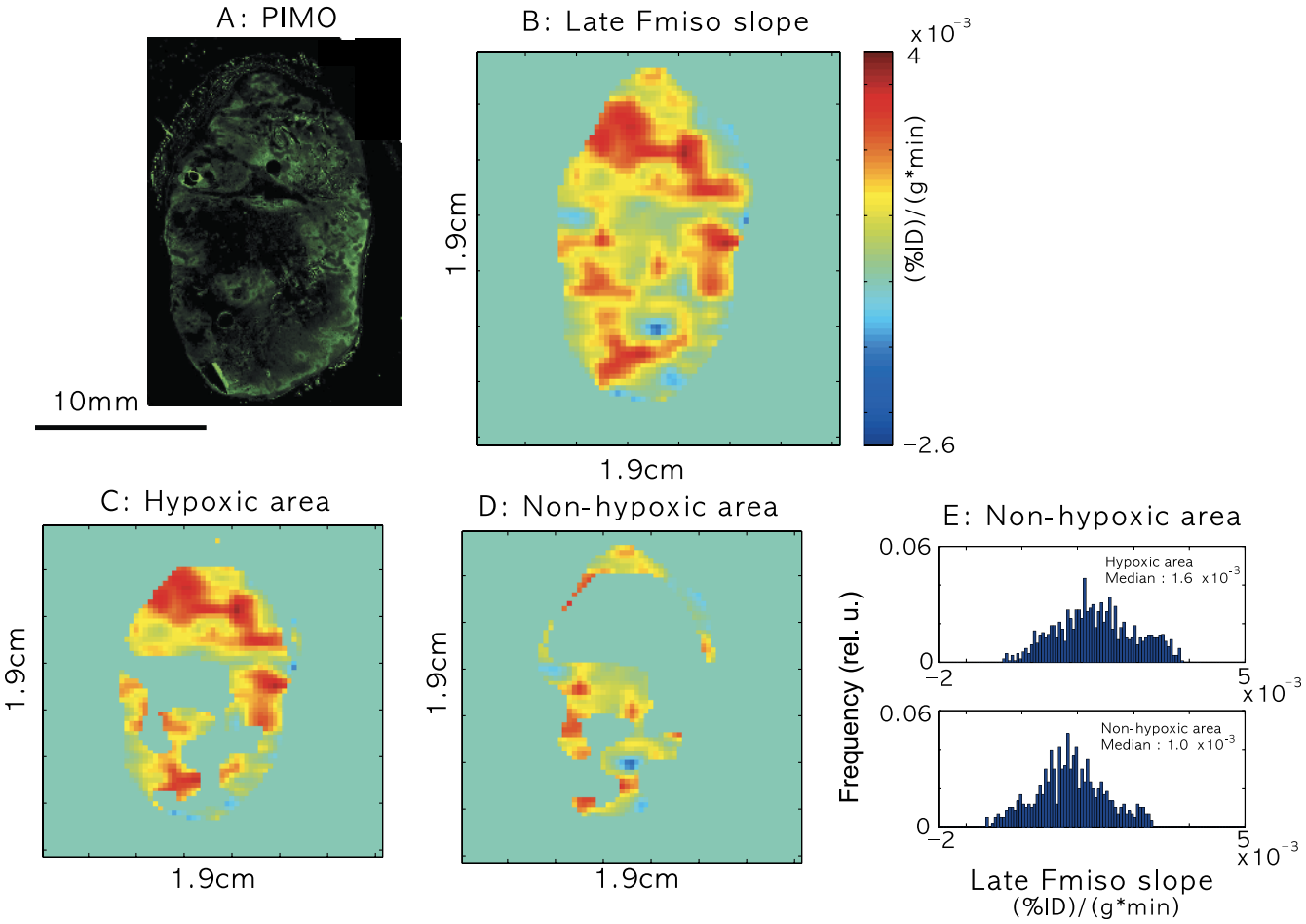

Figure W2. (A) Pimonidazole-stained (PIMO) section. (B) Late slope map of ^{18}F-Fmiso PET uptake curves. C and D are masked later ^{18}F-Fmiso PET slope values for hypoxic and nonhypoxic areas of the tumors, respectively. (E) Histogram plots of the late ^{18}F-Fmiso PET slope values for hypoxic and nonhypoxic areas of the tumors. The median values of later ^{18}F-Fmiso PET slope for hypoxic regions were significantly higher ($P < .001$) than those of nonhypoxic regions, but there was significant overlap. The tumor size was 870 mm^3.